Structural, magnetic and catalytic properties of perovskite-type mixed oxides LaMn$_{1-y}$Co$_y$O$_3$ (y = 0.0, 0.1, 0.3, 0.5, 0.7, 0.9, 1.0)

Gina Pecchi [a],*, Claudia Campos [a], Octavio Peña [b], Luis E. Cadus [c]

[a] *Facultad Ciencias Químicas, Universidad de Concepción, Casilla 160-C, Concepción, Chile*
[b] *Sciences Chimiques de Rennes, UMR 6226, CNRS, Université de Rennes 1, 35042 Rennes Cedex, France*
[c] *Instituto de Investigaciones en Tecnología Química (INTEQUI), UNSL-CONICET, Universidad Nacional de San Luis, Casilla 290, 5700 San Luis, Argentina*

Abstract

Substituted LaMn$_{1-y}$Co$_y$O$_3$ perovskite-type oxides ($0.0 \leq y \leq 1.0$), prepared by the citrate method, have been investigated as catalysts in the total combustion of acetylacetate. The characterization results indicate variation in specific surface area, crystal structure, infrared spectra and reducibility. The crystal phase transformation was found to occur for y_{Co} values above 0.5. The role of Mn is to stabilize the cobaltite structure, which does not tolerate more than 30% substitution of Co for Mn. The catalytic activity in the total combustion of acetylacetate can be related with changes in the crystal structure and specific surface area. The higher intrinsic activity of the cobaltite doped with 10 wt% Mn, $y_{Co} = 0.9$, can be explained by the changes in crystal and electronic properties. Magnetic properties (susceptibility, ZFC/FC and M-loops) show strong ferromagnetic interactions in the range ($0.0 < y_{Co} \leq 0.5$) while antiferromagnetism is progressively settled at higher cobalt concentrations.
© 2008 Elsevier B.V. All rights reserved.

Keywords: Manganese; Cobalt; Perovskites; Acetyl acetate

1. Introduction

Metal oxides with perovskite-type structure ABO$_3$ have been extensively studied as alternatives to noble metals catalysts for automotive emission control since the 1970s [1–3] because they are less expensive in comparison with their noble metal counterparts. The major drawback of large scale application of these structures lies in their low surface area and increased tendency to sinter. Among all perovskites functioning as complete oxidation catalysts, the best ones are compounds containing transition metals Mn, Fe, Co or Ni in the B-site [4], and the consequences of a partial substitution of the cation B by B′ of similar oxidation state and ionic radius could improve perovskite stability or enhance their redox efficiency [5,6]. This enhancement can be related with the perovskite crystal structure, and therefore, differences in crystal structure must be related with differences in catalytic activity. Indeed for LaMnO$_3$, it has been reported that the structure can be modified during the synthesis stage, depending on the oxygen pressure. If the oxygen pressure range is between $10^{-4.2}$ and $10^{-14.4}$ bar, the cubic stoichiometric structure is obtained [7]; if it is between 1 and $10^{-15.05}$ bar, perovskite obtained is not stoichiometric (LaMnO$_{3+\lambda}$) and it has orthorhombic symmetry. The rhombohedral structure, presented by LaCoO$_3$, is stable in an oxygen pressure range between 1 and 10^{-7} bar. Partial substitution at the A-site may also be responsible of off-stoichiometric effects, which depend on the nature of the B cation. It has been shown, for instance, that La$_{1-x}$Sr$_x$CoO$_{3-\delta}$ samples possess oxygen deficiencies whereas La$_{1-x}$Sr$_x$MnO$_{3+\delta}$ samples show oxygen over-stoichiometry [8].

The deviation from the ideal structure of a given perovskite can be estimated from the tolerance factor (t) introduced by Goldschmidt [9], calculated by:

$$t = \frac{(r_A + r_O)}{\sqrt{2}(r_B + r_O)} \quad (1)$$

where r_A, r_B and r_O are the ionic radii of A^{3+}, B^{3+} and O^{2-} ions, respectively, in the crystal. Although t is unity for an ideal cubic perovskite, this structure is also found for lower t-values ($0.75 < t < 1.0$). A value of $t < 1$ means compression of the B–O

* Corresponding author. Tel.: +56 41 2204324; fax: +56 41 2245974.
E-mail address: gpecchi@udec.cl (G. Pecchi).

bonds, while at the same time the A−O bonds are stretched. The structure can alleviate this tension with a cooperative turn of the octahedrons BO_6. When the tolerance factor is in an interval between $0.90 < t < 1.0$, the cooperative turn of the octahedrons principally results in rhombohedral structures, where the angle B−O−B is contracted and the tolerance factor is reduced. In the interval $0.75 < t < 0.9$, the cooperative turn of the octahedrons optimizes the distance A−O and produces a lengthening of the cell and the formation of a orthorhombic structure [10]. Nevertheless, in the case of the manganite compounds ($LaMnO_{3-\delta}$), another factor must be considered with regard to the structure distortion. Thus, the Jahn-Teller nature of the Mn^{3+} cation induces an additional axial distortion, which is cooperative in nature [11].

Even when the oxide activity is in general less than the catalyzers of supporting noble metals, activity comparable to supported Pd catalyzers in methane combustion has been reported for activated perovskites [12]. The catalytic activity of these oxides is principally related with the cation B. Since the activity increases through the series from Cr to Co, and the thermodynamic stability towards the reduction diminishes throughout the same sequence, the partial substitution of cation B by B′ of a similar ionic radius and oxidation state has been extensively studied. Thus, for $BaB_yB'_{1-y}O_{3+\lambda}$-type perovskites in which the B cation is Pb, Ce, Ti and the B′ cation is the metal Bi, Cu, Sb, the catalytic activity is related with the metal−O bond and the free reduction energy of the cations of site B, and a reaction mechanism based on the reducibility of cation B is proposed [13].

Additionally, Tabata et al. [14] studied the distinct electronic states of $LaMn_yCu_{1-y}O_{3+\lambda}$-type perovskites, concluding that the increase of the ionic character of the adsorbed oxygen is related with the network's non-stoichiometric oxygen and informing for the CO oxidation reaction that the increase in perovskite catalytic activity is explained by the change in the electronic structure of the adsorbed oxygen (O^-) as a consequence of the nature of cation B.

The possibility to substitute the B-site by another transition metal may have direct consequences over the magnetic properties of these materials either through the creation of oxygen deficiencies (or over-stoichiometry) or by direct transformation of the oxidation state of the substituted ion. In both cases, charge equilibrium associated to these processes will trigger strong magnetic interactions through the oxygen orbitals [15,16].

The La(Mn,Co)O₃ perovskite solid solution presented in this work is specially suited to look for such transformations. By substituting manganese by cobalt, the crystal structure is not greatly modified; however, any variation on the oxygen content will have a direct incidence on the reductive (or oxidative) capability of the material and, at the same time, will provoke a charge disequilibrium which will be immediately compensated by a transformation of the oxidation state of the Mn and/or the Co ions. In this way, we may optimize the intrinsic ferromagnetic properties due to the Co^{2+}/Mn^{4+} and Mn^{3+}/Mn^{4+} interactions over other inter-cationic interactions (Co^{2+}/Co^{3+}; Co^{3+}/Mn^{3+}) [17] and correlate them to the catalytic behaviour and the microstructure (specific area) of the material.

2. Experimental

2.1. Preparation

Pure cobaltite (LaCoO₃), manganite (LaMnO₃) and substituted $LaMn_{1-y}Co_yO_3$ (y_{Co} = 0.1, 0.3, 0.5, 0.7, 0.9) perovskites were prepared by the citrate method [18]. Stoichiometric amounts of an aqueous solution of the nitrates of the corresponding metals were added to an aqueous solution of citric acid with a 10% of excess over the number of ionic equivalents of cations. The resulting solution was stirred for 15 min at room temperature and slowly evaporated at 343 K under vacuum in a rotary evaporator until reaching gel formation. Then this gel was dried in an oven, slowly increasing the temperature up to 523 K and maintaining it overnight to yield a solid amorphous citrate precursor. The resulting powder was crushed and sieved to obtain the required particle size (<200 μm) and calcined at 973 K in air for 6 h.

2.2. Characterization

Chemical analysis of samples was determined by atomic absorption spectroscopy (AAS) using a PerkinElmer instrument model 3100. Samples were solubilised in a mixture of HCl and HNO_3 acids and then appropriately diluted to get concentrations of lanthanum, manganese and cobalt within the calibration range of the instrument. Specific areas were calculated using the BET method from the nitrogen adsorption isotherms, recorded at the temperature of liquid nitrogen on a Micromeritics apparatus Model ASAP 2010, taking a value of 0.162 nm^2 for the cross-sectional area of the N_2 molecule adsorbed at 77 K. Prior to the adsorption measurements, samples were outgassed at 423 K. X-ray powder diffraction (XRD) patterns of all calcined samples were obtained with nickel-filtered Cu $K\alpha_1$ radiation (λ = 1.5418 Å) using a Rigaku diffractometer controlled by a computer. XRD diffractograms were collected in the 2θ range 5–80°, in steps of 2° min^{-1}. Phase identification was carried out by comparison with the JCPDS-ICDD database cards. Temperature-programmed reduction (TPR) experiments were performed in a TPR/TPD 2900 Micromeritics system provided with a thermal conductivity detector. Samples of about 20 mg were placed in a U-shape quartz tube first purged in a synthetic air stream of 50 mL min^{-1} at 773 K for 1 h and then cooled to ambient temperature. Reduction profiles were then recorded by passing a 5% H_2/Ar flow at a rate of 40 mL min^{-1} while heating at a rate of 10 K min^{-1} from ambient temperature to 1173 K. Because the reduction profiles could be perturbed by experimental conditions [19,20], the operating variables (initial amount of reducible oxides (S_o), total flow rate (V^*), heating rate (β) and the initial H_2 concentration (C_o)) were chosen in such a way to measure the line profile and peak position accurately [21,22]. A cold-trap was placed just before the TCD of the instrument to remove the water from the exit stream. FTIR spectra were recorded in a Nicolet Magna-IR 550 instrument, equipped with a quartz sample holder with KBr windows. The perovskites were dehydrated at 483 K and finely ground in an agate mortar with KBr to obtain a sample/KBr ratio 1/150.

Magnetization ZFC/FC cycles were performed as a function of temperature between 2 and 300 K, using a Quantum Design MPMS-XL5 SQUID susceptometer. Samples were first cooled under no applied field; then, an external dc field of 0.025 T was applied at 2 K and samples were warmed up while recording the magnetization ZFC mode. Once at the maximum temperature, samples were cooled down under the same applied field (FC mode). In this way, any irreversibility in the magnetization is due to an ordered state settled at $T = T_{rev} = T_c$. Magnetization loops $M(H)$ at $T = 2$ K were performed on ZFC samples, between −5 and +5 T. Magnetic susceptibility was measured in the paramagnetic state ($T_c < T \leq 400$ K) under an applied field of 1 T.

2.3. Catalytic activity

The catalytic activity evaluation in the total combustion of acetyl acetate was performed in a conventional flow reactor at atmospheric pressure. In each experiment, 100 mg of catalysts diluted with 100 mg of silica as an inert was used. The activity was measured at different temperatures. The reactant mixture was fed into the reactor at 100 mL min^{-1}, measured at room temperature. Mass flow controller Brooks 5850E for an accurate and stable control of gas flow rates were used to prepare the feed mixture. It was bubbled through two thermostated and pressurised saturators containing acetylacetate. This stream was further mixed with O_2/He mixture in order to set a $C_4H_8O_2$:O_2:He = 1:10:89 molar mixture, preheated before enter to the reactor. In order to obtain a homogeneous temperature, the thermocouple was placed inside the reactor just at the beginning of the catalysts bed. The temperature was linearly increased up to the required temperature, and maintained constant for 30 min. Subsequently, it was raised to a new isothermal temperature using the same heating rate (1 K min^{-1}). Several isothermal steps were performed until reaching complete conversion. Reactor effluents were analyzed using an on-line gas chromatograph Hewlett Packard model HP 4890D with thermal conductivity detector. Helium was used as a carrier gas and the column used was a 30-m capillary Supelco 25462. A Quadrupole mass spectrometer Shimadzu, GCMS-QP5050 model was used to detect small traces of products.

3. Results and discussion

The elemental composition of the LaMn$_{1-y}$Co$_y$O$_3$-perovskite oxides was determined by atomic absorption spectrometry (AAS) and results are compiled in Table 1. It can be seen that cobalt and lanthanum contents approach nominal ones, although manganese content is somewhat lower than the theoretical composition for the manganite substituted with low contents of cobalt ($y_{Co} = 0.1$ and 0.3).

The BET specific surface areas of these samples are also summarised in Table 1. Manganite exhibits the largest BET value of 38.6 m^2 g^{-1}; and upon substitution, BET remains almost constant till $y_{Co} \leq 0.5$. For higher y_{Co} values, a progressive decrease occurs until reaching the cobaltite surface value of 16.3 m^2 g^{-1}.

The lowest value of the series is 8.4 m^2 g^{-1}, corresponding to the substituted perovskites with $y_{Co} = 0.9$.

The X-ray diffraction analysis of the LaMn$_{1-y}$Co$_y$O$_3$ oxides was performed with the objective to reveal the crystal structure and crystalline phases developed during the calcination step. To estimate the deviation from the ideal structure, the tolerance factor, t-values for the studied perovskites are shown in Table 1. A t-value between 0.78 and 0.81 is indicative that a cubic structure is predicted, although perhaps somewhat distorted, since rhombohedral and orthorhombic structure can be formed.

Fig. 1 displays the XRD patterns of LaMn$_{1-y}$Co$_y$O$_3$ oxides calcined at 973 K. For comparison purpose, the bar patterns of cubic LaMnO$_3$ (JCPDS, 750440), rhombohedral LaMnO$_{3.15}$ (JCPDS, 320484) and rhombohedral LaCoO$_3$ (JCPDS, 480123) phases are also included. It can be seen that all samples are single-phase perovskites. Manganite (LaMnO$_3$) and cobaltite (LaCoO$_3$) perovskites belong to cubic and rhombohedral phases, respectively, in agreement with the results reported in the literature [4,7]. A careful inspection of the diffraction profiles for the substituted perovskites reveals that these are distorted from their regular crystal structure. Thus, $y_{Co} = 0.1$ seems to fit better to a rhombohedral LaMnO$_{3.15}$ structure, because of the presence of a faint splitting at 33° (see below); $y_{Co} = 0.3$ fits with the diffraction pattern of a cubic LaMnO$_3$ structure with a slight shift towards larger 2θ angles due to lattice contraction upon substitution of Mn^{x+} ions in the lattice by Co^{x+} ions, therefore it can be concluded that a orthorhombic structure is present. For $y_{Co} = 0.5$, the diffraction profile is almost perfect with the cubic LaMnO$_3$ structure; for $y_{Co} = 0.7$ and 0.9, the diffraction profiles are quite similar to the LaCoO$_3$ rhombohedral structure, with a slight shift towards larger 2θ angles due to lattice contraction upon substitution of Co^{x+} ions in the lattice by Mn^{x+} ions.

These findings show that there is no apparent linear correlation between the perovskite structure and the substitution degree, and that for $y_{Co} > 0.5$, the transformation of the crystal phase occurs. The general trend in the substituted perovskites is the following: for $y_{Co} = 0.3$ and 0.5, the diffraction patterns correspond to a structural modification of the cubic manganite, therefore it can be concluded that these perovskites present the orthorhombic structure. For $y_{Co} = 0.7$ and 0.9, the diffraction patterns correspond to the modification of rhombohedral cobaltite. For $y_{Co} = 0.1$, a new geometric form is detected. A careful analysis of two important diffraction peaks ($2\theta = 33°$ and 57°) shows the changes in the crystalline structure of this series. A close up of the signal corresponding to $2\theta = 33°$ is also shown in Fig. 1. It can be observed that the two signals studied for the perovskites with $y_{Co} = 0.0$, 0.3 and 0.5 are singlets. The first, at 33° is acute and intense, while the one at 57° is wide and of much less intensity, typical of orthorhombic structures. The perovskite with $y_{Co} = 0.1$ presents different behaviour, indicating that the structure changes since the signal at 33° presents a small doublet and the singlet at 57° presents a shoulder at 58° characteristic of rhombohedral systems. For the perovskites with $y_{Co} = 0.7$, 0.9 and 1.0, the structure is rhombohedral. The lines of the values of $2\theta = 33°$ is an acute, very intense doublet that is separated for close to 0.02°, while the second one at the 57° presents a shoulder at 58° and is wide with low inten-

Table 1
Bulk composition (wt%), specific BET area, mean particle size (d) and tolerance factor (t) for LaMn$_{1-y}$Co$_y$O$_3$ perovskites

	y_{Co}	La[a]	Mn[a]	Co[a]	S_{BET} (m^2 g^{-1})	d (nm)	t
LaMnO$_3$	0.0	57.4 (57.4)[b]	22.5 (22.7)[b]	–	38.6	26.5	0.78
LaMn$_{0.9}$Co$_{0.1}$O$_3$	0.1	56.3 (56.3)[b]	18.4 (20.4)[b]	2.5 (2.4)[b]	38.6	31.2	0.78
LaMn$_{0.7}$Co$_{0.3}$O$_3$	0.3	56.2 (56.2)[b]	13.2 (15.8)[b]	6.5 (7.3)[b]	38.6	34.0	0.79
LaMn$_{0.5}$Co$_{0.5}$O$_3$	0.5	56.0 (56.0)[b]	10.1 (11.3)[b]	11.5 (12.1)[b]	30.0	26.2	0.79
LaMn$_{0.3}$Co$_{0.7}$O$_3$	0.7	56.8 (56.8)[b]	6.6 (6.7)[b]	18.0 (16.9)[b]	21.9	34.1	0.80
LaMn$_{0.1}$Co$_{0.9}$O$_3$	0.9	56.6 (56.6)[b]	2.3 (2.2)[b]	22.5 (21.6)[b]	8.4	50.1	0.81
LaCoO$_3$	1.0	56.5 (56.5)[b]	–	24.5 (24.0)[b]	16.3	60.5	0.81

[a] Estimated error is below 1%.
[b] Nominal values are in parentheses.
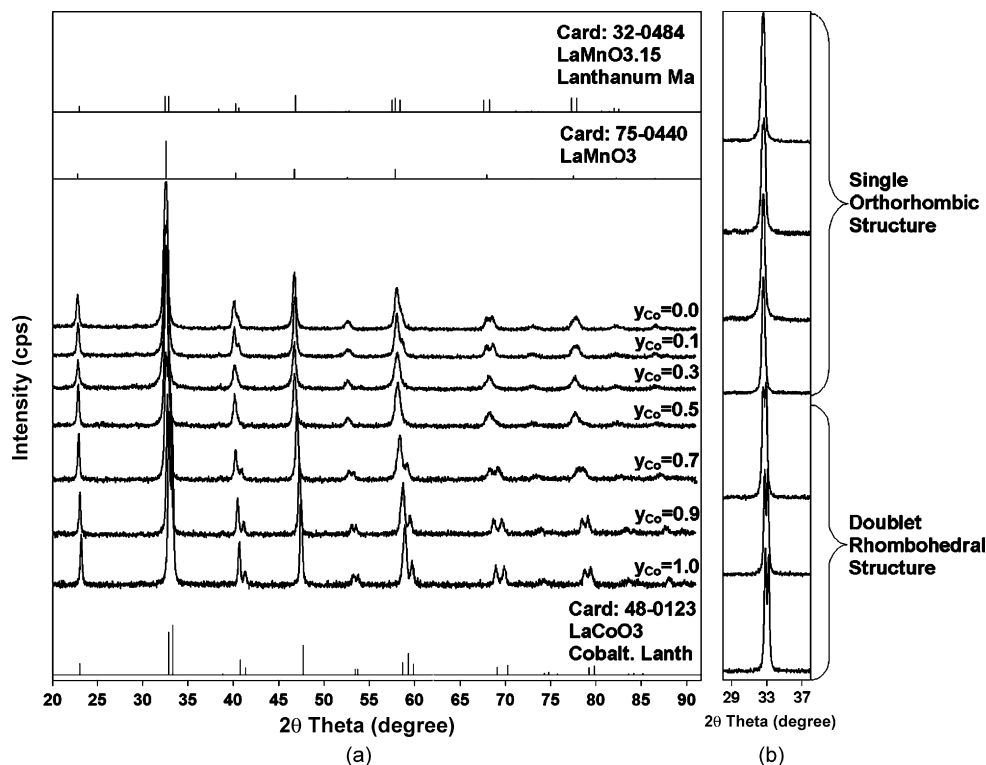
Fig. 1. XRD profiles for LaMn$_{1-y}$Co$_y$O$_3$.

sity. These results suggest that the perovskite with $y_{Co} = 0.1$ is formed with a mixture of LaMnO$_3$ and LaMnO$_{3.15}$ structures. For $y_{Co} = 0.3$, the structure corresponds to the cubic LaMnO$_3$ with some modifications that give it a structure with rhombohedral geometry [23]. The peak shift towards larger 2θ values upon increasing Co-content means that the unit cell volume increases with the Co-content. Provendier et al. [24] have attributed the linear dependence of the lattice parameters with the substitution degree. Fig. 2 shows the shift of the diffraction peaks of the 2θ values of 40.58°, 47.52° and 58.92° corresponding to the manganite structure as a function of the substitution degree. Two tendencies are clearly observed for values of $y_{Co} < 0.5$ and $y_{Co} > 0.5$. Different behaviours are observed for $y_{Co} = 0.5$. For values of $y_{Co} = 0.1, 0.3$, a somewhat linear tendency is observed with the degree of substitution. This result is explained considering that the cooperative turn of the octahedrons optimizes the A−O distance in these perovskites, producing a lengthening of the cell resulting in a orthorhombic structure. For the case of

$y_{Co} = 0.5$, it is notable that the diffractogram is practically equal to the one for $y_{Co} = 0.0$: the displacement with respect to the manganite structure is minimal. This result can be related with the cationic ordering when Mn and Co are found in equimolar quantities.
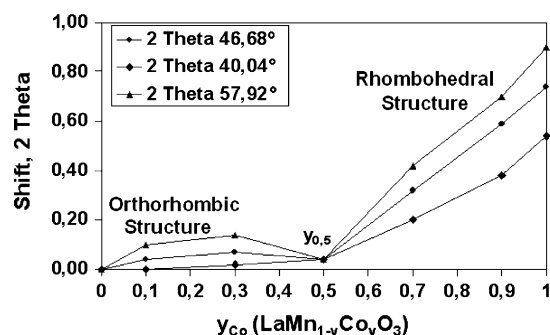
Fig. 2. Shift of three diffraction peaks as a function of y_{Co} for LaMn$_{1-y}$Co$_y$O$_3$.

For the case of $y_{Co} = 0.7$, 0.9 and 1.0, all are observed to present the same rhombohedral structure with a marked displacement with the degree of substitution. This result is explained considering that the insertion of Mn in the cobaltite produces a cooperative turn of the octahedrons in that the rhombohedral structure is maintained with a greater degree of distortion. In this structure, the angle B−O−B contracts, and consequently a marked displacement of the most intense signals is observed in the diffractograms. This large distortion of the structure for $y_{Co} = 0.7$ and 0.9 suggests that a certain proportion of separate, simple oxides should appear in parallel for these substitutions. The absence of diffraction lines belonging to single manganese or cobalt oxides can be taken as indicative that these oxide phases are highly dispersed or in an amorphous form.

All these findings should be correlated with the ionic radius of each one of the components. Presence of several ionic states (Mn^{3+}, Mn^{4+}, Co^{2+} and Co^{3+}) makes difficult to decide, from just the XRD data, which is the best combination of oxidation states to comply with charge equilibrium requirements. For this, a correlation with the magnetic data is necessary, as to be discussed later in this work. Several considerations can be forwarded, however, at this stage: first of all, it can be expected that, when substituting Mn^{3+} by Co, this ion enters the solid solution as Co^{2+}, leading to the formation of an equivalent amount of Mn^{4+} to preserve electroneutrality of the lattice. In such a case, the mean ionic radius of the B cation must show an increase, with an accompanying increase of the lattice volume. At the same time, because of the transformation $Mn^{3+} \rightarrow Mn^{4+}$, there is a progressive decrease of the amount of the Mn^{3+} Jahn-Teller cations, responsible of the lattice deformation which leads to the perovskite structure, resulting on an overall constant lattice volume, as suggested by Fig. 2, for $y_{Co} < 0.5$.

During the second half of the solid solution, i.e., for $y_{Co} > 0.5$, the increasing shift of the XRD lines suggests a systematic decrease of the lattice volume. This contraction correlates well with the presence of Co ions as Co^{3+} in a low spin (LS) state, for which the ionic radius is lower than the corresponding high spin (HS) state (Co^{3+}: HS, 0.61 and LS, 0.55 Å) [25]. The mean ionic radius of the B-site decreases and the tolerance factor should increase, as shown in Table 1. Again, this hypothesis is confirmed by the magnetic data presented further in this work.

Table 1 presents the particle size values for the entire series of studied perovskites. These sizes have been calculated using the Scherrer equation and the Warrens relation applied to the most crystalline and clear signal that appears at angle $2\theta = 46°$ of the Bragg equation [26]. The crystal size is observed to increase with the degree of substitution of Co, which indicates a tendency to form more crystalline perovskites. This is the expected result considering that the crystallinity and specific surface are properties that vary inversely proportional.

The vibration frequencies in the infrared are fundamental in the determination of crystalline structures [27]. The frequencies reported in the literature [28] generally are for cubic perovskites to which four vibration modes have been assigned: ν_1 = asymmetrical lengthening of the B−O bond of the structure's octahedrons BO_6; ν_2 = symmetrical lengthening of the
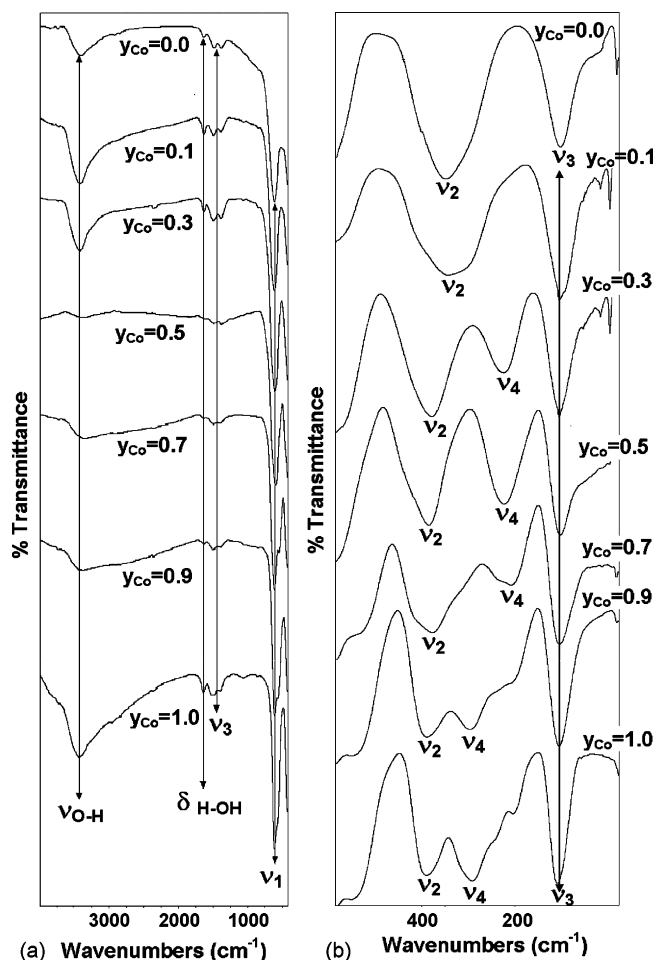

Fig. 3. FTIR spectra for $LaMn_{1-y}Co_yO_3$. (a) 4000–500 cm^{-1}; (b) 500–0 cm^{-1}.

O−B−O bond; ν_3 = vibration of the network's cation A against the octahedrons BO_6; ν_4 = deformation of the vibration angle of the O−B−O bond, which is not active in the infrared for cubic perovskites [29], but can be active for the perovskites that present deformations in the structure. Fig. 3a presents the IR spectra for all the perovskites in the zone between 4000 and 500 cm^{-1}, and Fig. 3b presents the IR spectra corresponding to the far zone. When the two figures are superimposed, four frequencies reported for the perovskites emerge. In Fig. 3a, the most important band of the perovskites structure, ν_1 is observed at 604 cm^{-1}, which is the characteristic band of oxides with perovskite-type structure. This band appears more acute for the perovskites with $y_{Co} = 0.0$ and 0.5, which correspond to more symmetrical structures. The widening of this band and/or the appearance of a shoulder indicates a structure with lower symmetry. In the perovskites with $y_{Co} \geq 0.7$, a shoulder also appears at 563 cm^{-1}, which is characteristic of this structure type. In Fig. 3a for the perovskites with $y_{Co} = 0.0$, 0.1, 0.3, a broad band is observed at 3200 cm^{-1} and a small band is observed at 1500 cm^{-1}. These two bands are assigned to La_2O_3 as $La(OH)_3$ and $La(CO_3)_3$, respectively. The cobaltite spectra for $y_{Co} = 1.0$ also presents a band at 2800 cm^{-1} assigned to carbonated segregated La_2O_3 phase. The spectra for perovskites with $y_{Co} = 0.5$, 0.7, 0.9 also insinuate the appearance of bands at 1495 and

$1377\,cm^{-1}$, which correspond to a vibration mode ν_3 of the CO_3^{2-} groups that are essentially asymmetrical and symmetrical lengthenings of the O–C–O bond [30] due to the presence of segregated phases in the form of carbonates. The wide band at $3600\,cm^{-1}$ is associated to the lengthening of water's O–H bond due to exposure to air and environmental humidity for the studied perovskites.

In Fig. 3b, the characteristic frequencies ν_2, ν_3 and ν_4 are observed with differences in band intensity, position, and appearance, which confirms the structural changes previously discussed for the series of studied perovskites. For the cobaltite, $y_{Co} = 1.0$, the spectra corresponds to a rhombohedral structure with great symmetry [14]. The band at $419\,cm^{-1}$ corresponds to the mode ν_2 and the band at $334\,cm^{-1}$ to ν_4, which is active for rhombohedral structures. The band that appears at low frequency, $176\,cm^{-1}$ corresponds to the vibration of the bond ν_3. With respect to manganite, $y_{Co} = 0.0$, the other extreme of the series, the spectra corresponds to a orthorhombic structure with great symmetry, in which three vibration modes reported for this structure type [31] appear. The wide, intense band at $383\,cm^{-1}$ corresponds to the vibration mode ν_2 and the band at $172\,cm^{-1}$ to the vibration mode ν_3. It is important to note that the vibration mode ν_4 is not active, as expected according to the structure determined by XRD. For $y_{Co} = 0.1$, the IR spectra is very similar to the manganite one. The XRD results indicate the presence of a mixture of orthorhombic and rhombohedral structures. Consequently with the absence of ν_4, it can be concluded that the orthorhombic structure with great symmetry predominates. The perovskites with $y_{Co} = 0.3$ and 0.5 present vibration modes ν_2 and ν_4, which are active but displaced towards lower vibration frequencies that determined the low symmetry in the network. For the case of perovskites with $y_{Co} = 0.7$ and 0.9, bands similar to those of cobaltite with rhombohedral structure are observed. In these perovskites, a slight displacement towards lower frequencies is also observed, allowing the conclusion that the insertion of Mn in the cobaltite generates lower network symmetry. These results allow the conclusion that the manganite tolerates Co insertion without large structural changes up to values of $y_{Co} \leq 0.3$. For $y_{Co} = 0.1$, a mixture of structures is produced. Additionally, the insertion of Mn into the cobaltite produces notable distortions in the cobaltite's highly symmetric rhombohedral structure for values of $y_{Co} = 0.7$ and 0.9. For the substituted perovskite with a value of $y_{Co} = 0.5$, the situation is the formation of a highly symmetric orthorhombic structure due to the presence of the same quantity of Co^{3+} and Mn^{3+} cations that can produce greater interaction resulting in network contraction.

Temperature-programmed reduction profiles were performed with the aim to study the reducibility of the prepared perovskites (Fig. 4). The procedure considered a reduction under H_2/Ar flow up to 973 K. A first reduction was observed between 523 and 723 K for all the perovskites and a second reduction was observed between 823 and 923 K for the perovskites with $y_{Co} = 0.7$, 0.9 and 1.0. The reduction at lower temperatures (623 K) corresponds to surface oxygen species, while the reduction at higher temperature (823 K) is attributed to the reduction of the cobaltite structure ($LaCoO_3 = 1/2\,La_2O_3 + CoO + 1/4\,O_2$).
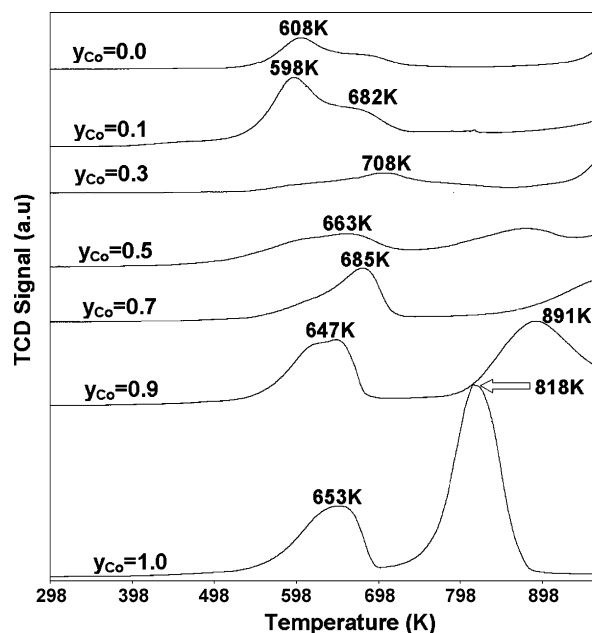

Fig. 4. Temperature-programmed reduction TPR for $LaMn_{1-y}Co_yO_3$.

Previous results do not report Co^{3+} spinel [32], and thus the segregated phase can be CoO and/or $CoCO_3$. A slightly different behaviour is found in the substituted perovskite with $y_{Co} = 0.1$, in which a broad peak with a shoulder is detected. This result can be interpreted assuming that this reduction peak corresponds to reduction of Mn^{3+} ions of $LaMnO_3$ to yield the $La_2Mn_2O_5$ phase that obviously implies an oxygen loss from the structure [24] (Fig. 4).

Marcos et al. [33] and Crespin and Keith [34] report that cobaltite reduction does not occur in a single step. At temperatures below 673 K, an intermediate with an oxygen-deficient perovskite structure is formed ($LaCoO_{3-\delta}$), corresponding to the first reduction peak in Fig. 4. The complete reduction of the perovskite, with formation of La_2O_3, $La(OH)_3$, H_2O and Co° corresponds to the second reduction peak at temperatures above 773 K. Another reduction mechanism, reported by Sis and Wirtz

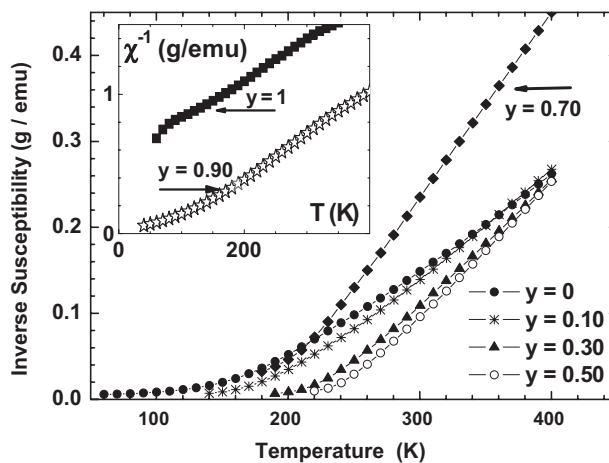Fig. 5. Inverse magnetic susceptibility measured under $H_{app} = 1\,T$ for $LaMn_{1-y}Co_yO_3$.

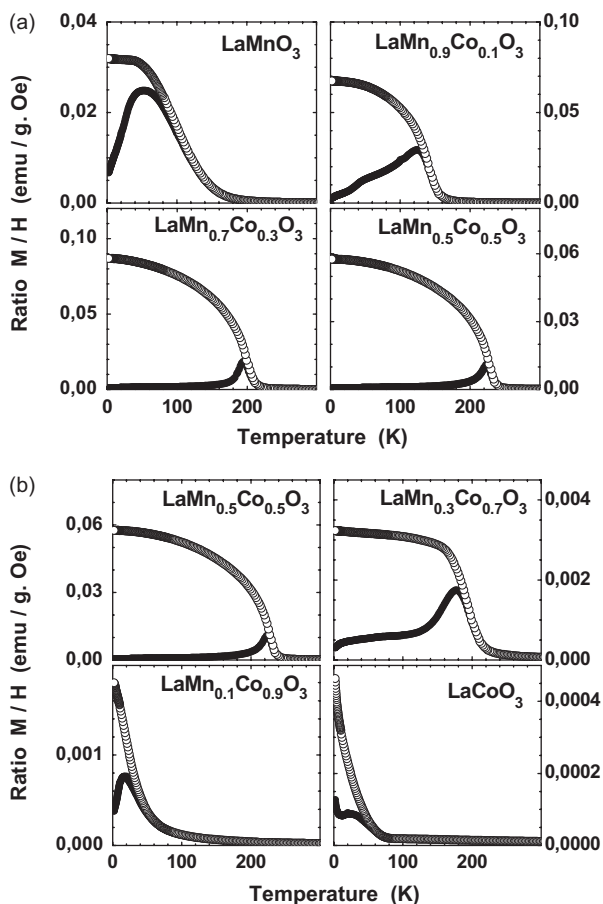Fig. 6. Magnetization cycles measured under 0.025 T (zfc: filled symbols; fc: open symbols) (a) $y_{Co} = 0.0$, 0.1, 0.3, 0.5; (b) $y_{Co} = 0.5$, 0.7, 0.9, 1.0 (sample $y_{Co} = 0.5$ is reported again for comparison with (a).

Table 2
Magnetic properties for $LaMn_{1-y}Co_yO_3$ perovskites

	y_{Co}	μ_{eff} (μ_B)	Θ (K)	T_c (K)
$LaMnO_3$	0.0	5.42	169	130
$LaMn_{0.9}Co_{0.1}O_3$	0.1	5.08	192	150
$LaMn_{0.7}Co_{0.3}O_3$	0.3	4.75	226	220
$LaMn_{0.5}Co_{0.5}O_3$	0.5	4.57	240	235
$LaMn_{0.3}Co_{0.7}O_3$	0.7	3.90	190	198
$LaMn_{0.1}Co_{0.9}O_3$	0.9	3.19	78	60
$LaCoO_3$	1.0	3.42	−195	65

perature range. The substituted perovskites with y_{Co} values of 0.3 and 0.5 present an intermediate behaviour and the temperature displacements are attributed to the previously discussed distortions.

The magnetic properties were investigated in the paramagnetic and in the magnetically ordered regimes, finding in both cases two well-identified regions separated by the equimolar composition $y_{Co} = 0.5$. The temperature dependence of the inverse magnetic susceptibility (Fig. 5) was analyzed by a classical Curie–Weiss relation $\chi = C/(T + \Theta)$ in the range $[1.5 \times T_c < T \leq 400 \text{ K}]$. For cobalt contents between $y_{Co} = 0$ and 0.5 (i.e., when cobalt substitutes Mn in the manganite $LaMnO_3$), the Curie–Weiss temperature Θ increases, with a smooth variation of the slope $|\Delta\chi^{-1}/\Delta T|$. For samples with $y_{Co} > 0.5$ (i.e., when Mn substitutes Co in the cobaltite $LaCoO_3$) the Curie–Weiss temperature Θ sharply decreases, reaching negative values at $y_{Co} = 1$. This non-monotonous variation is also observed in the ordering temperature T_c, which reaches a maximum value for $y_{Co} = 0.5$ (Table 2). The magnetic moment of the paramagnetic regime μ_{eff} ($\mu_{eff} = \sqrt{8 \times C}$) shows a linear decrease during the first half of the cobalt substitution, which is interpreted as the progressive transformation of Mn^{3+} into Mn^{4+} ions. This decrease gets sharper above $y_{Co} = 0.50$, since Mn ions are all converted into Mn^{4+}, and cobalt is being introduced as Co^{3+}, of lower effective moment and probable on a low or an intermediate spin state [15,39]. The overall behaviour observed through the compositional variation of the Curie–Weiss temperature Θ is explained by the varying character of the magnetic interactions between Co and Mn. During the first half of the series ($y_{Co} \leq 0.50$), strong Co^{2+}–Mn^{4+} double-exchange ferromagnetic interactions [40] are triggered when Co^{2+} is introduced into the lattice, while antiferromagnetism is advantaged when cobalt is introduced as Co^{3+} ($y_{Co} > 0.50$). These findings corroborate the assumptions drawn above from XRD data, and the information from the magnetic characterization should be better correlated with the structural changes observed by XRD and IR.

To investigate the ordered regime, two techniques were preferred: the thermal dependence (ZFC/FC cycles) and the field dependence (M-loops) of the magnetization. During warming (ZFC mode), a typical canted-type antiferromagnetic structure is observed [41], characterized by a pronounced peak in the magnetization, while on cooling (FC mode), the transition metal network orders at $T = T_c$, and the magnetization cycle becomes irreversible. Fig. 6a and b compares the regions separated by the equimolar composition $y_{Co} = 0.5$. A strong ferromagnetic

[35] points to intermediate formation, such as spinels of cobalt and manganese and lanthanum oxides. To determine the intermediates of the reduction, for $y_{Co} = 0.9$ and 1.0, after the first reduction peak, the reducing gas mixture was shifted to helium and the samples were cooled down to ambient temperature in helium flow. Immediately after they were analyzed by XRD and it was observed that the perovskite phase was preserved. The presence of segregated phases was not observed, consequently it can be concluded that the oxygen extracted transforms the perovskite structure into an oxygen-deficient one and that the extracted oxygen is converted into water [36]. The subsequent total reduction coincides with the results reported by Marcos and Crespin. Consequently, the displacement of this second peak at higher temperatures implies the stabilization of cobaltite due to insertion of Mn.

With respect to the manganite reduction profiles, $y_{Co} = 0.0$, Hirusta et al. [37] and Fierro et al. [38] also report two reductions. The first occurs where an oxygen-deficient intermediate $LaMnO_{3-\delta}$, is formed at 608 K, which is attributed to the only peak in the reduction for $LaMnO_3$ shown Fig. 4. The complete reduction of $LaMnO_3$ reported by Fierro occurs between 1173 and 1325 K with formation of the following reduction products, La_2O_3, $La(OH)_3$, MnO and H_2O. This reduction is not detected in Fig. 4 profiles since it is outside of the studied tem-
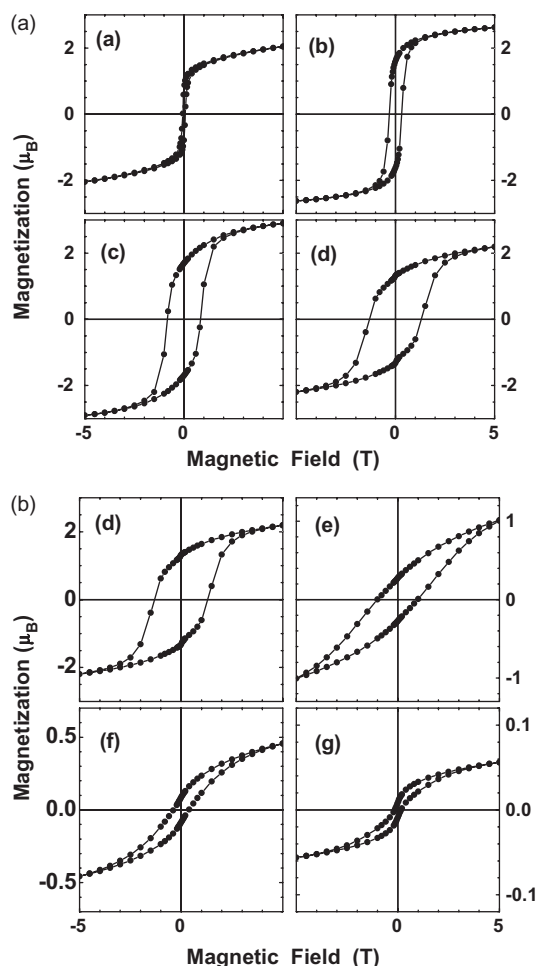
Fig. 7. Magnetization loops at $T = 2\,K$ for the solid solution $LaMn_{1-y}Co_yO_3$. (a) a) $y_{Co} = 0.0$, b) $y_{Co} = 0.1$, c) $y_{Co} = 0.3$, d) $y_{Co} = 0.5$ (notice identical Y-scales); (b) d) $y_{Co} = 0.5$, e) $y_{Co} = 0.7$, f) $y_{Co} = 0.9$, g) $y_{Co} = 1.0$ (sample $y_{Co} = 0.5$ is reported again for comparison with Fig. 7(a).

($\square$) $LaMnO_3$; ($\bullet$) $LaMn_{0.9}Co_{0.1}O_3$; ($\circ$) $LaMn_{0.7}Co_{0.3}O_3$; ($\blacklozenge$) $LaMn_{0.5}Co_{0.5}O_3$; ($\square$) $LaMn_{0.1}Co_{0.9}O_3$; ($\blacktriangle$) $LaMn_{0.3}Co_{0.7}O_3$; ($\blacksquare$) $LaCoO_3$

Fig. 8. Stationary-state conversion for $LaMn_{1-y}Co_yO_3$.

behaviour is observed for the first half of the series (Fig. 6a), since the magnetization M_{FC} reaches a characteristic plateau and the ordering temperature T_c increases towards a maximum value of 235 K. For y_{Co} compositions above 0.5, the magnetization decreases by one or two orders of magnitude, meaning that the ferromagnetic interactions Co^{2+}–Mn^{4+} are weaker (the quantity of Mn cations decreases), being progressively replaced by the less effective Co^{2+}–Co^{3+} interactions.

These qualitatively different behaviours are remarkably observed in the magnetization loops recorded at 2 K. For $y_{Co} \le 0.50$ (Fig. 7a), the magnetization $M(H)$ resembles an ideal squared-shape ferromagnetic loop, defined by a coercive field H_{coerc} (intersection at the X-axis) and a saturation magnetization ($M_{sat} = M$ at 5 T). The systematic increase of H_{coerc} with a slope of 2.6 T/at.Co, indicates an increasing number of ferromagnetic domains proportional to the number of pairs Co^{2+}/Mn^{4+}, all domains being fully ordered since M_{sat} stays constant. For $y_{Co} > 0.50$ (Fig. 7b), both H_{coerc} and M_{sat} decrease rapidly, reaching almost zero for the lanthanum cobaltite. In this case, $M(H)$ is undoubtedly a superposition of an antiferromagnetic behaviour and ferromagnetism, where the
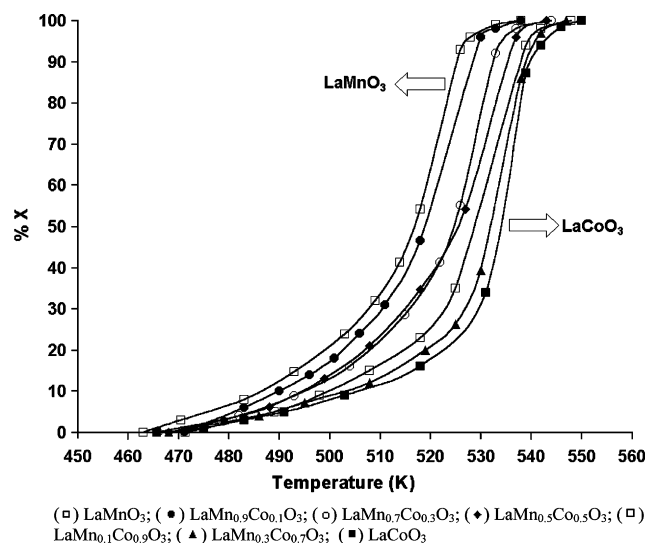
presence of Co^{3+} triggers antiferromagnetic interactions with Mn^{4+} and/or Co^{2+}.

Ethyl acetate is the most common solvent used in the printing industry. In these industries some mixtures of solvents are used, i.e., ethanol–ethyl acetate; toluene–ethyl acetate, etc., but in all cases ethyl acetate is present. All the $LaMn_{1-y}Co_yO_3$ perovskites were evaluated in total acetyl acetate combustion in a flow reactor under an excess of oxygen. Carbon dioxide, water and traces of acetaldehyde were detected. In no case was CO observed. The combustion profiles (space velocity = 60,000 $cm^3\,g^{-1}\,h^{-1}$) are displayed in Fig. 8, showing that total conversion is achieved at temperatures below 543 K. The ignition temperature (T_{50}), defined as the temperature required to obtain 50% conversion, is given in Table 3. Under the experimental conditions used, the lower ignition temperature (i.e., the higher activity) is displayed by manganite and the higher ignition temperature (i.e., lower activity) corresponds to cobaltite. The substituted perovskites display ignition temperatures between these two values, indicating that changes in y_{Co} values produce modification in the active sites required for organic compound oxidation. To clarify these trends, the catalytic activity informed as reaction rate and intrinsic activity (i.e., referred to catalyst weight (mmol $g^{-1}\,h^{-1}$) and to catalyst surface (mmol $m^{-2}\,h^{-1}$))

Table 3
Ignition temperature (T_{50}), reaction rate and intrinsic activity at 500 K and conversion less than 10%, in acetyl acetate combustion on $LaMn_{1-y}Co_yO_3$ perovskites

	y_{Co}	T_{ign}^{50} (K)	Reaction rate (mmol $g^{-1}\,h^{-1}$)	Intrinsic activity (mmol $m^{-2}\,h^{-1}$)
$LaMnO_3$	0.0	516	2.30	0.060
$LaMn_{0.9}Co_{0.1}O_3$	0.1	519	2.45	0.063
$LaMn_{0.7}Co_{0.3}O_3$	0.3	525	1.62	0.042
$LaMn_{0.5}Co_{0.5}O_3$	0.5	525	2.45	0.082
$LaMn_{0.3}Co_{0.7}O_3$	0.7	531	1.08	0.049
$LaMn_{0.1}Co_{0.9}O_3$	0.9	525	1.22	0.146
$LaCoO_3$	1.0	533	1.08	0.073

at 500 K and low conversion level (<10%) is also presented in Table 3. It can be seen that the reaction rate and the ignition temperature present the same trend with y_{Co} values: higher reaction rate for manganite and lower values for cobaltite. For the substituted perovskites, the behaviour is almost the same as exhibited for the ignition temperature, with no significant changes with respect to y_{Co} values. Still, when the intrinsic activity is compared, a different behaviour is detected. As can be observed in Table 3, manganite and cobaltite show almost the same values without significant differences with the perovskites with y_{Co} values of 0.1, 0.3 and 0.7. A noticeable increase in activity is detected for the substituted perovskite with $y_{Co} = 0.9$ and a slight increase in the intrinsic activity of $y_{Co} = 0.5$ can be detected.

Wu et al. [31] related the changes in the structural properties of perovskite-type solids, product of a isomorphic substitution of cation B with B′, with four parameters: (i) mass of cation B′, (ii) ionic radius of cation B′, and consequently the length of the B′−O bond, (iii) electronic structure of cation B′, and (iv) cation B′−O bond strength. All of these parameters are responsible for the structural, magnetic, and catalytic variations of the studied perovskites, and they can be classified in two categories. The first two are geometric and the last two are electronic. The geometric factors are considered in the calculation of factor *t*, reported in Table 1, and which present very similar values for the entire series of studied perovskites. Consequently, the catalytic characterization and activity results should be related with the electronic factors, which intervene directly in the crystalline structure formed. Still, it must be noted that catalysis is a surface science, and consequently the first stage of every heterogeneous catalytic reaction is the adsorption of the adsorbate on the adsorbent's surface.

Consequently, the higher reaction rate values obtained for $y_{Co} = 0.1$ and 0.5 (Table 3), are due to the adequate crystalline structure of these perovskite-type oxides. The notable increase in the intrinsic activity of perovskites with $y_{Co} = 0.9$ is because the catalytic activity at 500 K is obtained at a notoriously smaller surface area. Indeed, this perovskite, together with $y_{Co} = 0.5$, also presents more intrinsic activity than the rest of the series, and is the one that presents the two previously mentioned effects.

4. Conclusions

The substitution with Mn in $LaCoO_3$ perovskites does not modify the rhombohedral geometry up to $y_{Co} \geq 0.7$. Consequently, the substitution effect of y_{Co} in $LaMn_{1-y}Co_yO_3$ perovskites is related with notable changes in the crystalline structure and specific structure, and the IR results of this series are in line with crystal structure obtained by XRD. Ferromagnetic interactions are progressively settled when the cobalt concentration increases, as seen by an increase of the positive value of the paramagnetic Curie–Weiss temperature Θ and the ordering temperature T_c. For compositions above $y_{Co} = 0.5$, both characteristic temperatures decrease ($\Theta = -195$ K for $LaCoO_3$). The ordered state confirms the presence of two regimes, separated by the equimolar composition $LaMn_{0.5}Co_{0.5}O_3$: strong ferromagnetic Co^{2+}/Mn^{4+} and Mn^{3+}/Mn^{4+} interactions for $y_{Co} \leq 0.5$ and a superposition of

antiferromagnetism (mainly Co^{2+}/Co^{3+} and/or Co^{3+}/Mn^{3+}) and ferromagnetism for $y_{Co} > 0.5$.

References

[1] L.G. Tejuca, J.L.G. Fierro, J.M.D. Tascon, Adv. Catal. 36 (1989) 237.
[2] W.F. Libby, Science 171 (1971) 499.
[3] R.J.H. Voorhoeve, J.P. Remeika, D.W. Johnson, Science 180 (1973) 62.
[4] K. Poplawski, J. Lichtenberger, F. Keil, K. Schnitzlein, M. Amiridis, Catal. Today 62 (2000) 329.
[5] M.L. Rojas, J.L.G. Fierro, L.G. Trjuca, A.T. Bell, J. Catal. 124 (1990) 41.
[6] R. Sumathi, K. Johnson, B. Viswanathan, T.K. Varadarajan, Appl. Catal. A Gen. 172 (1998) 15.
[7] T. Nakamura, G. Petzow, L.J. Gauckeler, Mater. Res. Bull. 14 (1979) 649.
[8] J. Niu, et al., Catal. Today 126 (2007) 420.
[9] V.M. Goldschmidt, Skr. Nor. Viedenk.-Akad., Kl. I: Mat.-Naturvidensk. Kl., 1926, No. 8.
[10] G. Zheng, Y. Sun, X. Zhu, W. Song, Solid State Commun. 137 (2006) 326.
[11] J.B. Goodenough, Phys. Rev. 100 (1965) 564.
[12] M. Chen, X. Zheng, J. Mol. Catal. A: Chem. 221 (2004) 77–80.
[13] R. Sumathi, K. Johnson, B. Viswanathan, T. Varadarajan, Appl. Catal. A 172 (1998).
[14] K. Tabata, Y. Hirano, E. Suzuki, Appl. Catal. A 170 (1998) 245.
[15] S. Yamaguchi, Y. Okimoto, H. Taniguchi, Y. Tokura, Phys. Rev. B 53 (1996) R2926.
[16] Md. Motin Seikh, L. Sudheendra, C. Narayana, C.N.R. Rao, J. Mol. Struct. 706 (2004) 121.
[17] G. Blasse, J. Phys. Chem. Solids 26 (1965) 1969.
[18] P. Courty, H. Ajot, C. Marcilly, B. Delmon, Power Technol. 7 (1973) 21.
[19] N.Y. Vasanthacharya, P. Ganguly, C.N.R. Rao, J. Solid State Chem. 53 (1984) 140.
[20] A. Chainani, D.D. Sarma, I. Das, E.V. Sampathkumaran, J. Phys. Condens. Matter 8 (1996) L631.
[21] D.A.M. Monti, A. Baiker, J. Catal. 83 (1983) 323.
[22] P. Malet, A. Caballero, J. Chem. Soc. Faraday Trans. I 84 (1988) 2369.
[23] P. Ciambelli, S. Cimino, L. Lisi, M. Faticanti, G. Minelli, I. Pettiti, P. Porta, Appl. Catal. B 33 (2001) 193.
[24] H. Provendier, C. Petit, C. Estournes, S. Libs, A. Kienemann, Appl. Catal. A 180 (1999) 163.
[25] R.D. Shannon, Acta Crystallogr. A 32 (1976) 751.
[26] M. Bradford, M. Vannice, Appl. Catal. A: Gen. 142 (1996) 73.
[27] A. Davydov, Infrared Spectroscopy of Adsorbed Species on the Surface of Transition Metal Oxides, Wiley, England, 1990 (Chapter 1).
[28] E. Baran, Catal. Today 8 (1990) 133–151.
[29] N. Merino, B. Barbero, P. Grange, L. Cadús, J. Catal. 231 (2005) 232–244.
[30] R. Silverstein, G. Clayton, T. Morrill, Identificación espectrométrica de compuestos orgánicos, 2001, p. 115 (Chapter 3).
[31] Y. Wu, Z. Yu, S. Liu, J. Catal. 112 (1994) 157–160.
[32] J. Kirchnerova, M. Alifanti, B. Delmon, Appl. Catal. A: Gen. 231 (2002) 65.
[33] J. Marcos, G. Buitrago, A. Lombardo, J. Catal. 105 (1987) 95–106.
[34] M. Crespin, W. Keith, J. Catal. 69 (1981) 359–370.
[35] L. Sis, G. Wirtz, J. Appl. Phys. 44 (1973) 12.
[36] J. Petunchi, A. Lombardo, Catal. Today 8 (1990) 201.
[37] S. Hirusta, M. Pina, M. Menéndez, J. Santamaría, J. Catal. 179 (1998) 400–412.
[38] J.L.G. Fierro, J. Tascón, L. Tejuca, J. Catal. 89 (1984) 206–216.
[39] K. Knížek, Z. Jirák, J. Hejtmánek, M. Veverka, M. Maryško, G. Maris, T.T.M. Palstra, Eur. Phys. J. B47 (2005) 213.
[40] G. Blasse, J. Phys. Chem. Solids 26 (1965) 1969–1971.
[41] B. Dabrowski, X. Xiong, Z. Bukowski, R. Dybzinski, P.W. Klamut, J.E. Siewenie, O. Chmaissem, J. Shaffer, C.W. Kimball, J.D. Jorgensen, Short Phys. Rev. B 60 (1999) 7006.